

The Cosmic Ray Signature of Dark Matter Caustics

Roya Mohayaee¹, Pierre Salati²

¹*Institut d’Astrophysique de Paris (IAP), CNRS, UPMC, 98 bis boulevard Arago, France*

²*LAPTH, 9 Chemin de Bellevue, BP110, F-74941 Annecy-le-Vieux cedex, France*

emails: roya@iap.fr ; salati@lapp.in2p3.fr

6 February 2020

ABSTRACT

Gravitational collapse of dark matter, merger of dark matter haloes and tidal disruption of satellites are among processes which lead to the formation of fine and dense dark matter shells, also known as dark matter caustics. The putative weakly interacting species which may form the dark matter are expected to strongly annihilate in these dense regions of the Milky Way halo and generate in particular antiprotons and positrons. We derive the flux of these rare antimatter particles at the Earth and show that it depends significantly on the cut-off radius of the dark matter distribution at the galactic centre. Boost factors of ~ 30 are found with respect to a smooth NFW profile for high-energy antiprotons and low-energy positrons if this cut-off radius is taken to be 300 pc. Thus a promising window opens up for antiprotons around a hundred of GeV. However, dark matter caustics cannot provide a better explanation for the HEAT excess reported above ~ 10 GeV than a smooth NFW or isothermal cored distribution.

preprint no: LAPTH-1235/08

1 INTRODUCTION

The halo of our galaxy is believed to have formed from the gravitational collapse of dark matter (DM) and a continuous merger with other haloes. The formation of haloes, described by the Jeans-Vlasov-Poisson equation, proceeds with the formation of dark matter *shells*, also referred to as dark matter *caustics* (Sikivie & Ipser 1992; Sikivie et al. 1997; Tremaine 1999; Alard & Colombi 2005; Natarajan & Sikivie 2006). As the density peaks collapse under self-gravity, at the surfaces of (formally) infinite density where dark matter streams meet, caustics emerge. The infalling satellites are also disrupted by a similar mechanism. As a satellite moves inside the potential well of its host halo, a tidal tail forms, and around the apapsis of the orbit high-density shells or caustics emerge [see *e.g.* Hayashi et al. (2003)]. Since each infalling satellite also has his own caustics, the hierarchical formation of structures yields a hierarchy of caustics. Observational examples for the caustics are the shell galaxies, where shells of stars form during the merger of galaxies, by a mechanism very similar to the formation of dark matter caustics (Malin & Carter 1980; Carter et al. 1982; Hernquist & Quinn 1988, 1989).

Once formed, they cannot be destroyed : caustics are frequent structures in real and in phase space and remain permanent as long as there is continuous accretion. However, their over-density with respect to the background density can diminish with time due to continuous increase in the

number of streams. Therefore, it is likely that we are surrounded by a large number of fossil shells of disrupted satellites. The density of the shells can exceed that of the diffuse background by an amount which depends on the number of times the satellite has wrapped around our galaxy. Due to their vicinity and over-density, these shells can be important for dark matter search experiments.

The nature of dark matter remains a mystery. Supersymmetry and extra-dimension extensions of the standard electroweak model provide a natural candidate in the form of a weakly interacting and massive particle (hereafter WIMP). These species should fill up the galactic halo. If dark matter consists of WIMPS then they are expected to strongly annihilate in the dense regions of our halo (*i.e.* in the caustics) and generate in particular gamma-rays and charged cosmic rays such as positrons and antiprotons. Indeed, due to their very short diffusion length, positrons can be excellent tracers of nearby caustics. Although the implication of substructures, or surviving satellites, in boosting the cosmic-ray signal has been studied extensively [see *e.g.* Lavalle et al. (2007a); Lavalle et al. (2007b)], the signature of dark matter caustics on cosmic-rays has been rarely considered.

Here, we propose to study the boost in positron and antiproton signals due to annihilation in dark matter shells. The ideal way to pursue this study would be to use a very high-resolution simulation, however, even the latest simulations have not yet achieved a high enough resolution to identify the caustics in a typical galaxy, although, impressive progresses are being made (Vogelsberger et al. 2007). Analytic models for the formation of caustics are mainly based on the self-similar secondary infall (Fillmore & Goldreich

arXiv:0801.3271v1 [astro-ph] 21 Jan 2008

1984; Bertschinger 1985). We use a generalized version of the secondary infall model which takes into account the finite velocity dispersion of DM (Mohayaee & Shandarin 2006). Although secondary infall model has serious limitations because of the assumption of spherical symmetry and smooth accretion and because it ignores the hierarchical scenario of structure formation, it has so far provided a paradigm for the study of dark matter haloes [*e.g.* see Ascasibar et al. (2007)].

In Section 2, we review and generalize the secondary infall model for dark matter with finite velocity dispersion and give an analytic fit for the density profile which includes the caustics for a typical galaxy like our own. The cosmic ray signature of dark matter caustics is studied in Section 3 for large antiproton and positron horizon radii. In Section 4, the possibility of detecting a nearby caustic through its short range positron signal is investigated. We finally conclude in Section 5.

2 THE SECONDARY INFALL OR SELF-SIMILAR ACCRETION MODEL

Analytic evaluation of the halo density profile, and the prediction of the existence of caustics inside these structures, started with the works of Gott (1975) and Gunn (1977). With the main objective of explaining the flattening of the rotation curves of the galaxies, they considered the formation of a dark matter halo from the infall of matter onto an already-formed galaxy (or in later works onto a spherical overdense region). In an Einstein-de Sitter Universe a spherical over-density expands and then turns around to collapse. After collapse and at late times, the fluid motion becomes self-similar : its form remains unchanged when length are re-scaled in terms of r_{ta} , the radius of the shell which is currently turning around and collapsing. Physically self-similarity arises because gravity is scale-free and because mass shells outside the initial over-density are also bound and turnaround at successively later times. Self-similar solutions give power-law density profiles whose exact scaling properties depend on the initial condition, the central boundary conditions and on whether the fluid is collisionless or collisional (Fillmore & Goldreich 1984; Bertschinger 1985). The global density profile is a power-law which for suitable choices of initial conditions provides an explanation of the flattening of the rotation curves of the galaxies. A density profile of r^{-2} results for the galactic-scale fluctuations. However, the density profile is convolved with many spikes (*i.e.* caustics) of *formally* infinite densities which are rendered finite mainly by the velocity dispersion of dark matter.

In this model, the initial perturbation is assumed to be scale free, *i.e.*

$$\delta = \frac{\delta M}{M} \propto M^{-\epsilon} \quad \text{at} \quad t = t_i \quad . \quad (1)$$

Such scale-free perturbations result naturally in cosmological models with scale-free initial spectra. For a power-law spectrum $P(k) \sim k^n$, the mass variance $\sigma(M)$ scales as $M^{-(n+3)/6}$, which yields

$$\epsilon = \frac{n+3}{6} \quad . \quad (2)$$

As more and more mass shells turn around and collapse, the mass of halo grows at a rate of $t^{2/3\epsilon}$. The problem exhibits similarity solution *asymptotically* and can be solved numerically. The numerical solutions confirm the theoretical results which have been obtained assuming adiabatic invariance (Fillmore & Goldreich 1984). Asymptotically, the density profile reaches the power-law :

$$\rho = \begin{cases} r^{-2} & ; \quad \epsilon \leq \frac{2}{3} \\ r^{-9\epsilon/(1+3\epsilon)} & ; \quad \epsilon \geq \frac{2}{3} \end{cases} \quad (3)$$

For galactic-scale fluctuations ($n \sim 1.2$ as given by the galaxy-galaxy correlation function) one has $\epsilon \sim 0.2 - 0.3$. Here, we set $\epsilon = 0.2$, also for the purpose of comparing a few of our results with Fillmore & Goldreich (1984). The evolution equation, namely Newton's equation of motion written in self-similar variables, is ¹

$$\begin{aligned} \frac{d^2\lambda}{d\xi^2} + \left(\frac{1}{3} + \frac{4}{9\epsilon}\right) \frac{d\lambda}{d\xi} + \left(\frac{2}{3} + \frac{2}{9\epsilon}\right) \left(\frac{2}{9\epsilon} - \frac{1}{3}\right) \lambda \\ = -\frac{2}{9\lambda^2} \exp\left(\frac{2}{3\epsilon}(\epsilon-1)\xi\right) M(\lambda) \quad , \end{aligned} \quad (4)$$

where

$$\lambda = \frac{r}{r_{ta}} \quad \text{and} \quad \xi = \ln\left(\frac{t}{t_{ta}}\right) \quad . \quad (5)$$

The dimensionless radius λ is given in terms of the physical radius r and present turnaround radius r_{ta} and ξ is the dimensionless time given in terms of the turnaround time t_{ta} for each particle. Equation (4) has been solved with the initial condition given at $\xi = 0$ (corresponding to $t = t_{ta}$)

$$\lambda = 1 \quad \text{and} \quad \frac{d\lambda}{d\xi} = -\frac{8}{9} \quad , \quad (6)$$

with a prior knowledge of the mass $M(\lambda)$. The solution has been obtained iteratively : following an initial guess for $M(\lambda)$, equation (4) is integrated, then $M(\lambda)$ is evaluated, and the procedure is continued until the desired level of convergence is achieved. Here, we take a simpler approach. At small values of λ ($\lambda \ll 1$), mass becomes a power-law $M(\lambda) \approx \lambda$ (Fillmore & Goldreich 1984). We thus fit $M(\lambda)$ for $\epsilon = 0.2$ by the following profile

$$\frac{M(\lambda)}{M_{ta}} = \frac{\lambda}{1+\lambda} \quad , \quad (7)$$

where $M_{ta} = (3\pi/4)^2$. The solutions are shown in Fig. 1 for two choices of ϵ .

The density profile is given by

$$\frac{\rho}{\rho_b} = \frac{\pi^2}{8\lambda^2} \sum_j (-1)^j \exp\left(-\frac{2}{3\epsilon}\xi_j\right) \left(\frac{d\lambda}{d\xi}\right)_j^{-1} \quad , \quad (8)$$

where ρ_b is the cosmological background density which we take to be $1.6 \times 10^{-6} \text{ GeV cm}^{-3}$ and t_{ta} is the turnaround time of the particle that is at the j th point where $\lambda = \lambda(\xi)$ [see Bertschinger (1985) for further explanation].

The density (8) is evaluated numerically and plotted in Fig. 2. Evidently, the density profile is convolved with many spikes, namely caustics, where the density formally

¹ This is equation (23) of Fillmore & Goldreich (1984), rewritten in variables (5) [also used in Bertschinger (1985)].

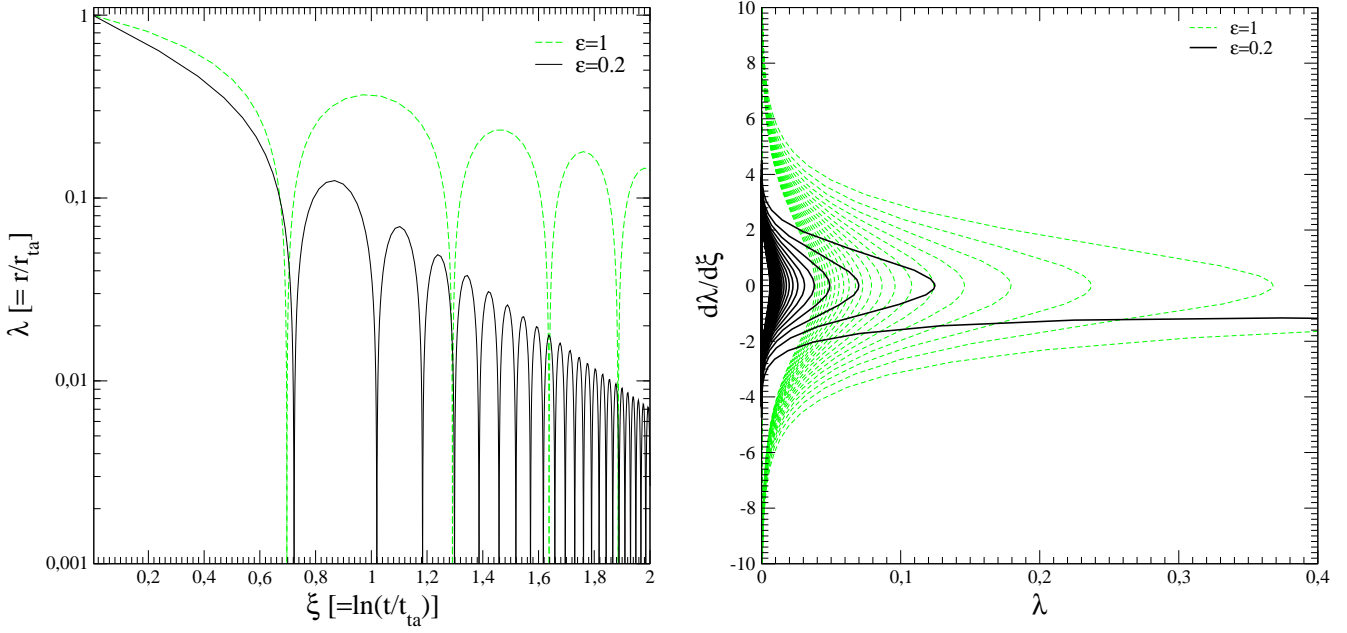


Figure 1. Particle trajectories in real and phase spaces are shown for two values of the parameter ϵ where λ is the non-dimensional radius and ξ is the non-dimensional time.

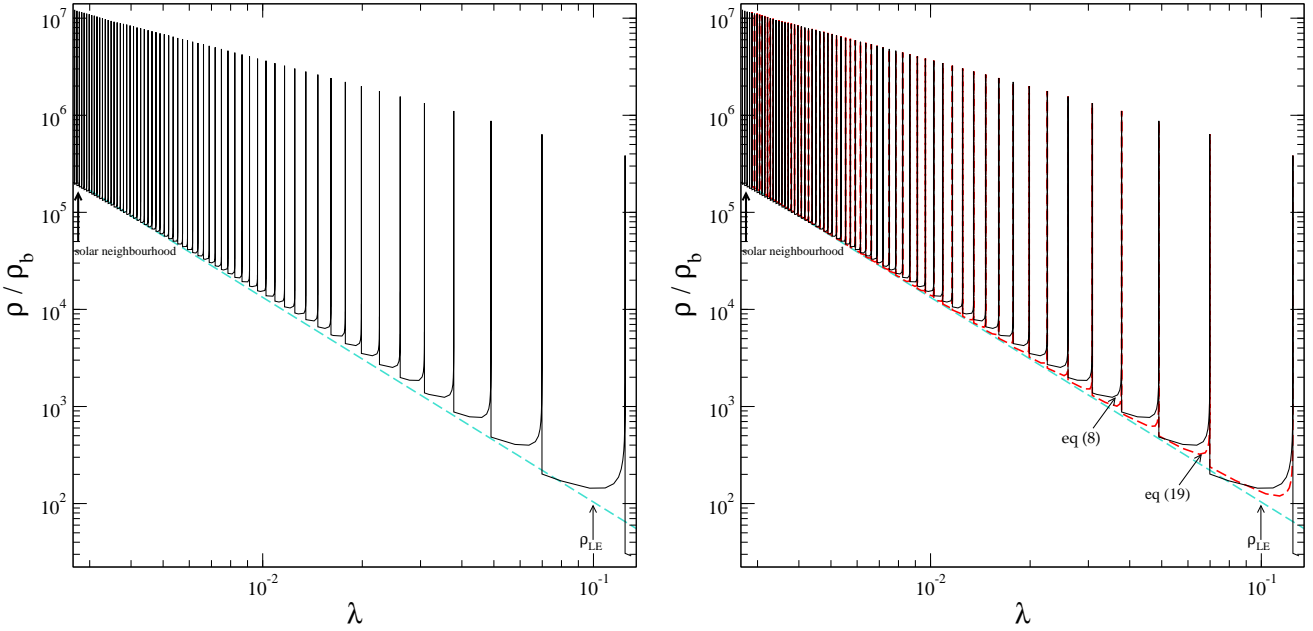


Figure 2. The left panel features the total numerically-obtained density for $\epsilon = 0.2$ [solid black curve, using expression (8)]. This solution is compared in the right panel to our analytic fit [dashed red curve, using expression (19)].

diverges. However, there is a natural cut-off to the density of the caustics due to the finite velocity dispersion of dark matter (Mohayaee & Shandarin 2006). For a generic value of ϵ , the thickness of the caustic shell may be expressed as

$$\Delta\lambda_k = \frac{(3\pi)^{2/3}}{4} e^{(P-1/3)\xi_k} \Lambda_k \frac{t\sigma(t)}{r_{\text{ta}}} . \quad (9)$$

The maximum density at the caustic positions is given by

$$\rho_{k,\text{max}} = \frac{G_k}{\sqrt{|\Delta\lambda_k|}} \rho_b = \frac{2G_k e^{(1-3P)\xi_k/6}}{(3\pi)^{1/3} \sqrt{-\Lambda_k}} \sqrt{\frac{r_{\text{ta}}}{t\sigma(t)}} \rho_b , \quad (10)$$

where

$$G_k = \frac{9P\pi^2}{32\sqrt{-2\lambda_k'}} \frac{e^{(6-9P)\xi_k/3}}{\lambda_k^2} , \quad (11)$$

and

$$P = \frac{2}{3} \left(1 + \frac{1}{3\epsilon} \right) , \quad (12)$$

whereas ρ_b is the cosmological background density, t is the age of the Universe, σ is the present-day velocity dispersion of dark matter particles which is that at decoupling re-scaled

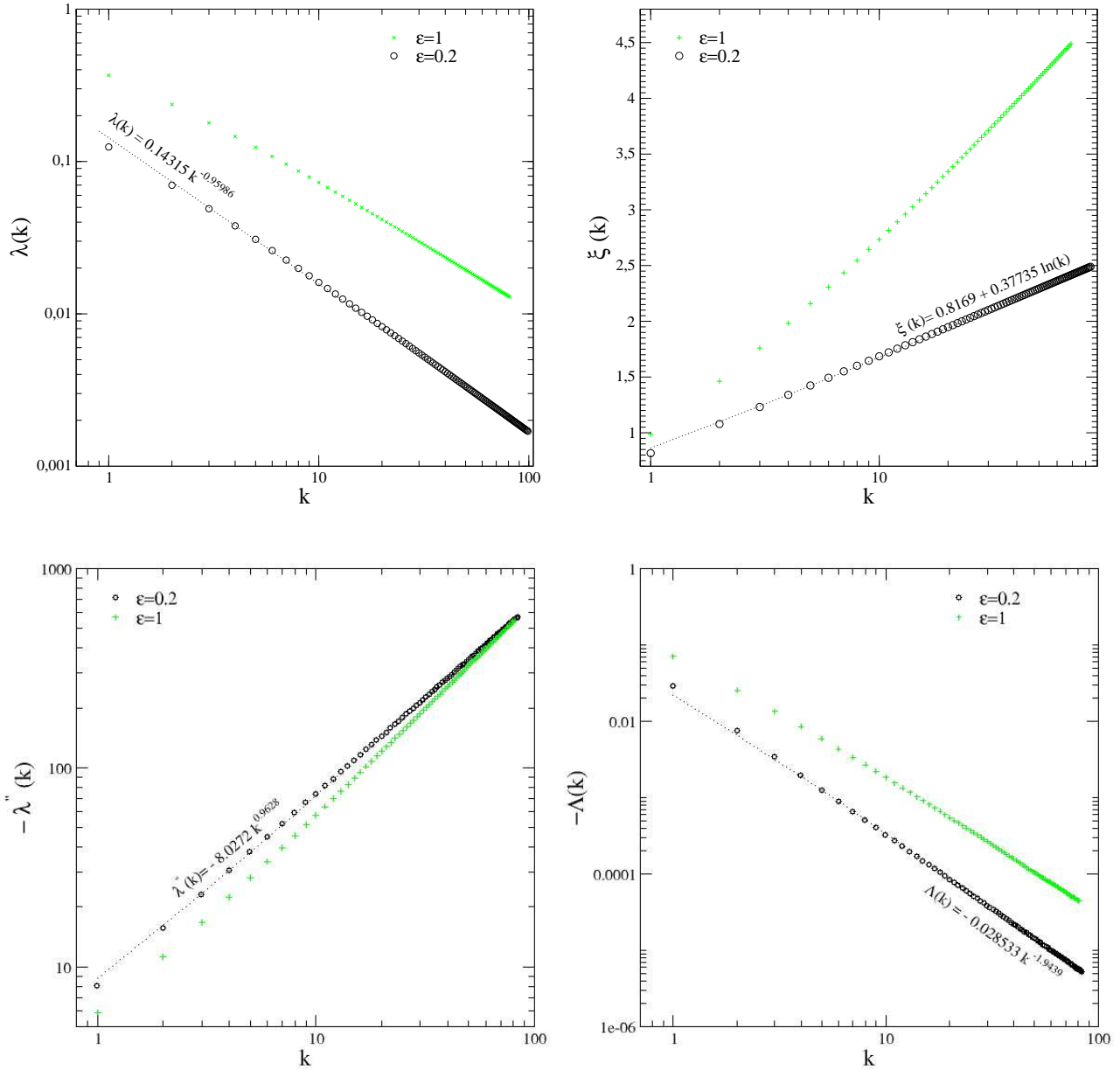


Figure 3. The dotted lines are the fittings [presented in expressions (14) to (17)] to numerical results from integration of the differential equation (4). The black open circles and the green crosses correspond respectively to $\epsilon = 0.2$ and $\epsilon = 1$.

with the expansion factor and $\xi_k = \ln(t/t_{ta})$ is the dimensionless time given in terms of the turnaround time t_{ta} of the particle that is now in caustic k . The first ten values of these parameters are listed in Table 1, assuming a velocity dispersion σ of 0.03 cm s^{-1} .

The density profile of caustics is simply given by

$$\rho_k = \begin{cases} \rho_{k,\max} & \lambda_k - |\Delta\lambda_k| \leq \lambda \leq \lambda_k \\ \sqrt{\frac{|\Delta\lambda_k|}{\lambda_k - \lambda}} \rho_{k,\max} & \lambda_{k+1} \leq \lambda \leq \lambda_k - |\Delta\lambda_k| \end{cases} \quad (13)$$

For $\epsilon = 0.2$, the four caustic parameters can be obtained

for all caustics from the following fits (see also Fig. 3) :

$$\lambda_k = 0.14315 k^{-0.95986} , \quad (14)$$

$$\xi_k = 0.8169 + 0.37735 \ln(k) , \quad (15)$$

$$\lambda_k'' = \left(\frac{d^2\lambda}{d\xi^2} \right)_k = -8.0272 k^{0.9628} , \quad (16)$$

$$\Lambda_k = -0.028533 k^{-1.9439} . \quad (17)$$

Similar fits can be obtained for other values of ϵ . The lower envelope (LE) of the density curve (dashed blue curve in Fig. 2) is fitted by

$$\frac{\rho_{LE}}{\rho_b} = 0.80527 \lambda^{-2.1093} . \quad (18)$$

k	ξ_k	λ_k	λ'_k	Λ_k
1	0.86369	0.12460	-8.8	-0.0222
2	1.09899	0.06987	-16.2	-0.0066
3	1.24000	0.04899	-23.4	-0.0032
4	1.34200	0.03782	-30.5	-0.0019
5	1.42200	0.03083	-37.6	-0.0012
6	1.48800	0.02604	-44.6	-0.0009
7	1.54499	0.02254	-51.6	-0.0007
8	1.59399	0.01988	-58.6	-0.0005
9	1.63800	0.01778	-65.5	-0.0004
10	1.67700	0.01608	-72.5	-0.0003

Table 1. The caustic parameters, for $\epsilon = 0.2$, obtained from numerical solution of (4) for the first ten caustics. Analytic fits (14)-(17) reproduce these results and give their values for the rest of the inner caustics.

Hence the total density curve can be fitted using the above expression together with the expressions (13) for the density profile ρ_k of the peaks, *i.e.*

$$\rho = \rho_{LE} + \rho_k . \quad (19)$$

In the right panel of Fig. 2, the above analytic fit is featured by the dashed red curve while the true density (8) from the numerical solution to (4) corresponds to the solid black curve. The fitted density profile is an excellent description of caustics even if it differs slightly from the true density profile far from the caustics.

3 THE COSMIC RAY SIGNAL OF DARK MATTER CAUSTICS

(i) Cosmic ray propagation : the salient features

Supersymmetry and extra-dimension extensions of the standard electroweak model provide a natural candidate for dark matter in the form of a weakly interacting and massive particle (hereafter WIMP). These species should fill up the galactic halo. They should also annihilate in pair and produce a host of particles among which are rare cosmic rays such as antiprotons and positrons. The production rate $q(\mathbf{x}, E)$ of these antimatter particles depends on their energy E and is related to the WIMP annihilation cross section σ_{ann} through

$$q(\mathbf{x}, E) = \eta \langle \sigma_{\text{ann}} v \rangle \left\{ \frac{\rho(\mathbf{x})}{m_\chi} \right\}^2 f(E) . \quad (20)$$

The coefficient η is a quantum factor equal to 1/2 for a self-conjugate particle like a Majorana fermion or to 1/4 otherwise. In what follows, we borrow our examples from supersymmetry and set $\eta = 1/2$. The annihilation cross section is averaged over the momenta of the incoming DM particles to yield $\langle \sigma_{\text{ann}} v \rangle$ whose value depends on the specific microscopic interactions at stake. The WIMP mass is denoted by m_χ . Finally, the energy distribution of the positrons dN_{e^+}/dE_{e^+} or of the antiprotons $dN_{\bar{p}}/dE_{\bar{p}}$ produced in a single annihilation is generically denoted by $f(E)$.

Whatever the source mechanism, charged cosmic rays subsequently propagate through the galactic magnetic field and are deflected by its irregularities : the Alfvén waves. In the regime where the magnetic turbulence is strong (which is the case for the Milky Way) cosmic ray transport needs

to be investigated numerically. Monte Carlo simulations (Casse et al. 2002) indicate that it is similar to space diffusion with a coefficient

$$K(E) = K_0 \beta \mathcal{R}^\delta , \quad (21)$$

which increases as a power law with the rigidity $\mathcal{R} = p/q$ of the particle. In addition, because the scattering centres drift inside the Milky Way with a velocity $V_a \sim 20$ to 100 km s^{-1} , a second order Fermi mechanism is responsible for some mild diffusive re-acceleration. Its coefficient K_{EE} depends on the particle velocity β and total energy E and is related to the space diffusion coefficient $K(E)$ through

$$K_{EE} = \frac{2}{9} V_a^2 \frac{E^2 \beta^4}{K(E)} . \quad (22)$$

In the case of positrons, diffusive re-acceleration is completely dominated by energy losses. Finally, galactic convection wipes cosmic rays away from the disc with a velocity $V_C \sim 5$ to 15 km s^{-1} .

After this short digest of cosmic ray transport, we can write the master equation fulfilled by the space and energy distribution function $\psi = dn/dE$ as

$$\begin{aligned} \partial_z (V_C \psi) - K \Delta \psi + \\ + \partial_E \left\{ b^{\text{loss}}(E) \psi - K_{EE}(E) \partial_E \psi \right\} = q(\mathbf{x}, E) . \end{aligned} \quad (23)$$

This equation applies to any species (protons, antiprotons or positrons) as long as the rates for production q and energy loss $b^{\text{loss}}(E)$ are properly accounted for. It has been solved within the framework of the semi-analytical two-zone model which has been extensively discussed in previous works (Maurin et al. 2001; Donato et al. 2001) and whose salient features we briefly recall now. According to our approach, a steady state is assumed and the region of the Galaxy inside which cosmic rays diffuse (the so-called diffusive halo or DH) is pictured as a thick disc which matches the circular structure of the Milk Way [as shown in Fig. 2 of (Maurin et al. 2002)]. The galactic disc of stars and gas, where primary cosmic rays are accelerated, lies in the middle. It extends radially 20 kpc from the centre and has a half-thickness h of 100 pc. Confinement layers where cosmic rays are trapped by diffusion lie above and beneath this thin disc of gas. The intergalactic medium starts at the vertical boundaries $z = \pm L$ as well as beyond a radius of $r = R \equiv 20$ kpc. Notice that the half-thickness L of the diffusive halo is not known and reasonable values range from 1 to 15 kpc. The diffusion coefficient K is the same everywhere whereas the convective velocity is exclusively vertical with component $V_C(z) = V_C \text{ sign}(z)$. The galactic wind, which is produced by the bulk of the disc stars like the Sun, drifts away from its progenitors along the vertical directions, hence the particular form assumed here for V_C . Notice also that the normalization coefficient K_0 , the index δ , the galactic drift velocity V_C and the Alfvén velocity V_a are all unknown. This situation may be remedied with the help of the boron to carbon B/C ratio which is quite sensitive to cosmic ray transport and which may be used as a constraint. The three propagation models featured in Table 2 have been borrowed from Donato et al. (2004). The MED configuration provides the best fit to the B/C measurements whereas the MIN and MAX models lead respectively to the minimal and maximal

Case	δ	K_0 [kpc ² /Myr]	L [kpc]	V_C [km/s]	V_a [km/s]
MIN	0.85	0.0016	1	13.5	22.4
MED	0.70	0.0112	4	12	52.9
MAX	0.46	0.0765	15	5	117.6

Table 2. Typical combinations of diffusion parameters that are compatible with the B/C analysis (Maurin et al. 2001). As shown in (Donato et al. 2004), these propagation models correspond respectively to minimal, medium and maximal primary antiproton fluxes.

allowed antiproton fluxes which can be produced by WIMP annihilation.

The solution of the master equation (23) may be generically expressed as the integral

$$\psi(\odot, E) = \int dE_S \int_{\text{DH}} d^3 \mathbf{x}_S G(\mathbf{x}_\odot, E \leftarrow \mathbf{x}_S, E_S) q(\mathbf{x}_S, E_S). \quad (24)$$

The energy E_S at the source runs over a range which depends on the nature of the cosmic ray species as discussed below. The space integral is performed over the diffusive halo. The convolution (24) involves the Green function G which describes the probability for a cosmic ray that is produced at location \mathbf{x}_S with the energy E_S to reach the Earth where it is detected with the degraded energy E . The cosmic ray space and energy density ψ can be translated into the differential flux $\Phi \equiv \beta \psi / 4\pi$ where β stands for the particle velocity. This flux is expressed in units of particles $\text{m}^{-2} \text{s}^{-1} \text{sr}^{-1} \text{GeV}^{-1}$ and can be written as the product

$$\Phi(\odot, E) = \mathcal{F} \int dE_S f(E_S) I(E, E_S), \quad (25)$$

where the information related to particle physics has been factored out in

$$\mathcal{F} = \eta \frac{\beta}{4\pi} \langle \sigma_{\text{ann}} v \rangle \left\{ \frac{\rho_\odot}{m_\chi} \right\}^2. \quad (26)$$

The energy distribution $f(E_S)$ describes the spectrum at the source and depends in our case on the details of the WIMP annihilation mechanism. The information on the galactic DM density profile ρ as well as on the propagation of cosmic rays within the Milky Way is summarized in the halo integral

$$I(E, E_S) = \int_{\text{DH}} d^3 \mathbf{x}_S G(\mathbf{x}_\odot, E \leftarrow \mathbf{x}_S, E_S) \left\{ \frac{\rho(\mathbf{x}_S)}{\rho_\odot} \right\}^2, \quad (27)$$

where the solar neighbourhood DM density is denoted by ρ_\odot . The halo integral $I(E, E_S)$ plays a crucial role in the derivation of the flux at the Earth of the antimatter species that are produced inside the galactic DM halo by WIMP annihilations. The reach of the Green function G depends on the nature of the cosmic ray particle (either positrons or antiprotons) and on the energies E and E_S . This range delineates the region of the Milky Way from which most of the signal detected at the Earth originates. It corresponds to the extension of the so-called horizon beyond which the Green function is suppressed. The horizon plays a crucial role in the subsequent discussion as it may or may not reach down to the centre of the Milky Way and probe its dense DM content.

Except for high-energy positrons, the horizon is much larger than the separation between adjacent caustics for

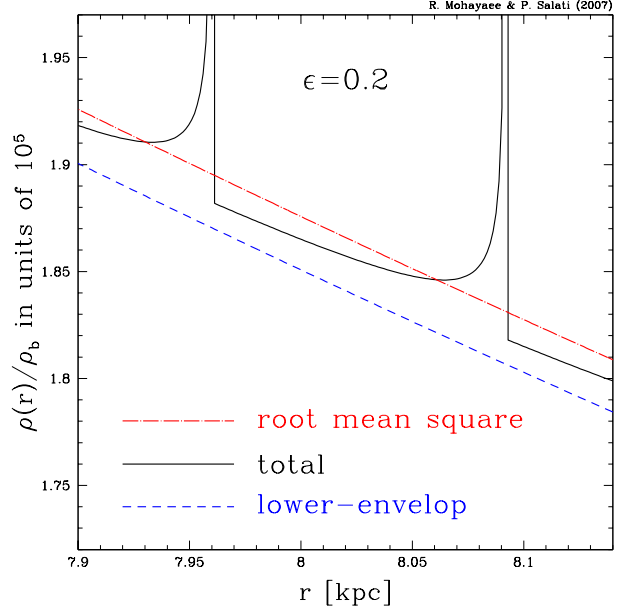


Figure 4. Typical DM density in the self-similar accretion model of Section 2. The solar system is located at $r_\odot = 8$ kpc from the galactic centre and is surrounded by two nearby thin shells. The long-dashed dotted red curve features the root mean square density used in the calculation of the halo integral $I(E, E_S)$ whereas the short-dashed blue line corresponds to the lower envelope ρ_{LE} .

which we find a typical distance of ~ 130 pc in the solar neighbourhood. If the DM halo of our Galaxy results from the self-similar accretion which we have discussed in Section 2, the WIMP density that enters in the DH integral (27) is given by the sum of the lower envelope density (18) and the caustic density (13). The latter varies by several orders of magnitude at the crossing of each shell as shown in Fig. 2. Because the typical scale over which the Green function G changes appreciably is much larger than the shell thickness Δr_k and the shell separation $r_k - r_{k+1}$, we may actually average the density ρ_k of the k^{th} caustic over the distance extending from the inner radius r_{k+1} to the outer boundary r_k . This leads respectively to the linear average

$$\overline{\rho}_k = \rho_{k, \text{max}} (2\sqrt{\epsilon_k} - \epsilon_k), \quad (28)$$

as well as to the quadratic average

$$\overline{\rho}_k^2 = \rho_{k, \text{max}}^2 \{ \epsilon_k (1 - \ln \epsilon_k) \}. \quad (29)$$

where $\epsilon_k = \Delta \lambda_k / (\lambda_k - \lambda_{k+1})$. The DM density squared that enters in the halo integral $I(E, E_S)$ may be expressed as the average

$$\overline{\rho^2} \equiv \rho_{\text{LE}}^2 + 2\rho_{\text{LE}} \overline{\rho}_k + \overline{\rho}_k^2. \quad (30)$$

Halo model	α	β	γ	r_s [kpc]
Cored isothermal (Bahcall & Soneira 1980)	2	2	0	4
Navarro, Frenk & White (Navarro et al. 1997)	1	3	1	25

Table 3. Parameters for different dark matter density profiles [equation (31)] for the Milky Way.

The corresponding root mean square density is featured in Fig. 4 as a function of the galactocentric distance r (long-dashed dotted red curve) together with the actual DM density $\rho_{\text{LE}} + \rho_k$ (solid black line) and the short-dashed blue lower envelope ρ_{LE} . The turnaround radius r_{ta} has been determined by requiring that the linearly averaged DM density $\bar{\rho} \equiv \rho_{\text{LE}} + \bar{\rho}_k$ is equal to a solar neighbourhood value of $\rho_{\odot} = 0.3 \text{ GeV cm}^{-3}$. We infer a turnaround radius r_{ta} of 2.7854 Mpc. The solar system is located between the 58th and 59th shells whose inner densities reach a maximum value $\rho_{\text{max}} = 1.16 \times 10^7 \rho_b$ of 18.6 GeV cm^{-3} . These caustics are extremely thin though, and we find $\Delta\lambda_{58}/(\lambda_{58} - \lambda_{59}) \sim 10^{-8}$ with a shell separation of 132 pc and a shell thickness of $\Delta\lambda_{58} = 4.74 \times 10^{-13}$.

(ii) The positron signal

The WIMPs which annihilate inside the thin and highly concentrated DM shells of the Milky Way halo are expected to yield an a priori much higher positron or antiproton flux at the Earth than in the more conventional case of a smooth DM galactic distribution. Previous investigations have concentrated essentially on the models listed in Table 3 for which the DM profile is generically given by

$$\rho(r) = \rho_{\odot} \left\{ \frac{r_{\odot}}{r} \right\}^{\gamma} \left\{ \frac{1 + (r_{\odot}/r_s)^{\alpha}}{1 + (r/r_s)^{\alpha}} \right\}^{(\beta-\gamma)/\alpha}. \quad (31)$$

The galactocentric distance r_{\odot} of the solar system has been set equal to 8 kpc. The isothermal cored distribution (Bahcall & Soneira 1980) features a constant DM density within the inner 4 kpc whereas the Navarro, Frenk and White profile [Navarro et al. (1997) hereafter NFW] diverges like r^{-1} at the galactic centre. Other numerical investigations (Diemand et al. 2004) find a DM profile index γ of 1.16 ± 0.14 in good agreement with the NFW result and should lead to the same positron or antiproton flux at the Earth. In order to compare the positron signal $\Phi_{\text{shell}}(\odot, E)$ from DM caustics to the flux $\Phi_{\text{smooth}}(\odot, E)$ yielded by the DM distributions of Table 3, we should compute their ratio. The positron and antiproton signals from annihilating WIMPs have already been thoroughly investigated in the literature and shown to depend on both the assumed DM distribution and the specific features of the particle physics model selected to describe the DM species. Our aim is here to gauge solely the influence of the DM shells on the anti-matter cosmic ray signal and to investigate whether or not the annihilation of WIMPs is enhanced inside the caustics and leads to a larger signal than in the case of an isothermal cored profile or a NFW cusp.

Because the flux depends on the spectrum $f(E_S)$ at the source, we have decided to concentrate on the halo integral $I(E, E_S)$ which encodes specifically the information on both the DM distribution and the cosmic ray propagation.

Positrons essentially diffuse on the irregularities of the magnetic field and lose energy through synchrotron radiation and inverse Compton scattering on the cosmic microwave background radiation and on the galactic starlight. The energy loss rate $b^{\text{loss}}(E)$ increases with the energy E as

$$b^{\text{loss}}(E) = E_0 \epsilon^2 / \tau_E, \quad (32)$$

where $\epsilon = E/E_0$ and $E_0 = 1 \text{ GeV}$. The typical energy loss timescale is $\tau_E = 10^{16} \text{ s}$ and may be combined (Lavalle et al. 2007a; Delahaye et al. 2007) with the diffusion coefficient $K(E)$ to yield the typical diffusion length

$$\lambda_D = \sqrt{4K_0 \tilde{\tau}}. \quad (33)$$

The parameter K_0 is the normalization of the diffusion coefficient whilst $\tilde{\tau} = \tilde{t}(E) - \tilde{t}(E_S)$ is the typical time (including both energy losses and diffusion) during which the positron energy decreases from E_S to E . As shown by Baltz & Edsjö (1999), the positron energy E may be translated into the pseudo-time

$$\tilde{t}(E) = \tau_E \left\{ \frac{\epsilon^{\delta-1}}{1-\delta} \right\}, \quad (34)$$

where δ denotes the spectral index of the diffusion coefficient K . The diffusion length λ_D is actually the extension of the positron sphere. It gauges how far positrons travel before being detected at the Earth. A rapid inspection of equation (34) indicates that λ_D increases as the detected energy E decreases except for energies E_S at the source very close to E . It is well known that the positron sphere is fairly reduced at high energies, say above $\sim 100 \text{ GeV}$, whereas it extends over several kiloparsecs below 10 GeV.

The transition occurs between 10 and 100 GeV as featured in the left panel of Fig. 5 where the positron boost, which we define as

$$B_{e^+} \equiv I_{\text{shell}}^{e^+}(E, E_S) / I_{\text{smooth}}^{e^+}(E, E_S), \quad (35)$$

is plotted as a function of the positron energy E at the Earth (*i.e.* after propagation and energy loss) for a fixed value of the injection energy E_S . This situation arises in particular for Kaluza-Klein species which may annihilate directly into electron-positron pairs. The injection energy E_S is equal to the WIMP mass m_{χ} and a value of 1 TeV has been chosen here. The solid and long-dashed curves correspond respectively to the NFW profile and to the isothermal cored distribution of Table 3. The DM shell density is derived from relation (30) and is very close to the lower envelope density ρ_{LE} . The latter diverges at the galactic centre with a profile index of $\gamma \simeq 2.11$. This divergence is not physical and the DM shell density should eventually reach a plateau below some cut-off radius $r_{\text{cut-off}}$. Actually, the self-similar accretion model of Section 2 cannot predict an infinite number of shells since the formation of the Milky Way DM halo took place ~ 10 billion years ago. The innermost shell should lie at a radius $r_{\text{cut-off}}$ and should delineate a core inside which the density is uniform. Notice also that baryons have been disregarded although they could play a crucial role in the inner regions of the DM halo. We have therefore assumed that the shell density (30) reaches a plateau below an unknown radius $r_{\text{cut-off}}$. This cut-off radius is a free parameter of our analysis and three values are featured in Fig. 5. For energies at the Earth exceeding $\sim 100 \text{ GeV}$, the positron sphere is

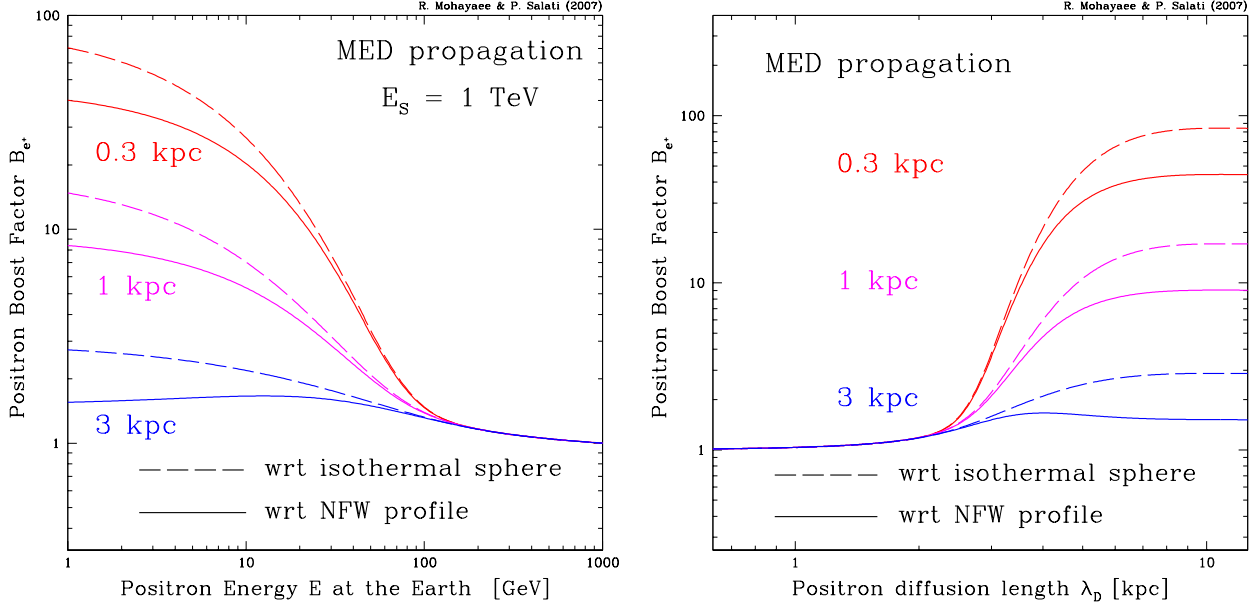


Figure 5. Positron boost factor in the presence of DM caustics normalized to a NFW profile (solid) or an isothermal cored distribution (long-dashed) in the case of the propagation model MED of Table 2. In the left panel, a positron line at $E_S = 1$ TeV has been assumed and B_{e^+} is plotted with respect to the energy E at the Earth. In the right panel, the boost factor is featured as a function of the diffusion length λ_D . Three different values for the cut-off radius of the DM shell distribution have been considered.

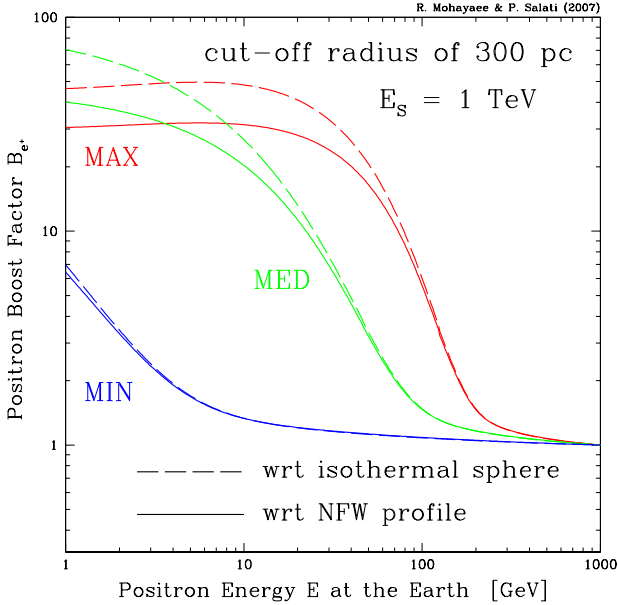


Figure 6. Same as before but in the case of a cut-off radius of 300 pc and for the three propagation models of Table 2.

reduced and the positron signal probes only the solar neighbourhood where the DM density is always equal to ρ_\odot . The halo integrals $I^{e^+}(E, E_S)$ are identical whatever the underlying model for the DM density profile. As expected, the positron boost factor is approximately equal to unity. Below ~ 100 GeV, the positron sphere widens as E decreases and consequently as λ_D gets larger. Because DM is more abundant in the shell scenario than what is expected in the

case of the smooth profiles of Table 3, the positron boost increases as the energy E goes down from 100 GeV to 1 GeV. This trend is particularly pronounced for the isothermal sphere (long-dashed curves) for which the DM abundance is the smallest in the inner parts of the Milky Way. The boost factor is shifted downwards (solid lines) by a factor of ~ 2 when a NFW profile is now considered. As the cut-off radius is decreased from 3 kpc down to 300 pc, the shell DM density gets larger at the galactic centre and so does the boost as is clear in Fig. 5. Notice finally that the true argument of the halo integrals I^{e^+} is the diffusion length λ_D which combines the energies E and E_S . The right panel, where the positron boost B_{e^+} is presented as a function of λ_D , is therefore a mere translation of the left plot. Because the diffusion length increases as the energy E at the Earth goes down, the panels of Fig. 5 are somewhat symmetrical.

The solid and long-dashed red curves of the right panel correspond to a cut-off radius of 300 pc. These curves have been plotted in Fig. 6 as a function of the diffusion length λ_D for the three different propagation models of Table 2. In the MAX configuration, the spectral index δ is the smallest and the pseudo-time $\tilde{t}(E)$ is most sensitive to the energy E as expected from relation (34). This trend is strengthened by a large diffusion coefficient K_0 . The positron horizon probes the galactic centre as soon as the energy E at the Earth gets lower than ~ 50 GeV. The same regime is reached for an energy of ~ 10 GeV in the case of the MED model whereas the positron sphere never extends to the galactic centre in the MIN case even for energies at the Earth as low as 1 GeV.

(iii) The antiproton signature

The propagation of cosmic ray antiproton is dominated by diffusion. Energy losses as well as diffusive re-acceleration do not play any major role. A very crude approximation for the

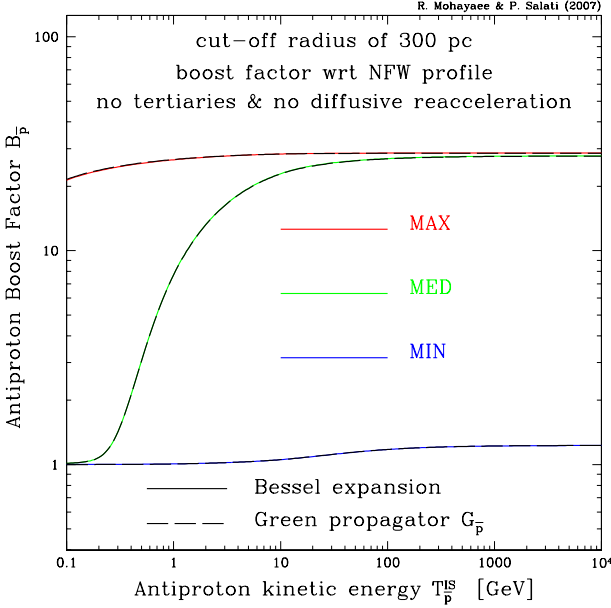


Figure 7. Antiproton boost factor $B_{\bar{p}}$ in the presence of DM caustics with respect to a NFW profile. A cut-off radius of 300 pc has been assumed for the shell distribution. The three propagation models of Table 2 are featured. The boost factor is plotted as a function of the interstellar antiproton energy $T_{\bar{p}}^{\text{IS}}$. The Bessel expansion technique (long-dashed) and the Green method (solid) lead to identical results.

antiproton Green function is obtained by neglecting galactic convection and solving the resulting Poisson equation in infinite space. This yields the antiproton propagator

$$G_{\bar{p}}(\mathbf{x}_{\odot} \leftarrow \mathbf{x}_S) \equiv \frac{1}{4\pi K(E)} \frac{\delta^3(\mathbf{x}_{\odot} - \mathbf{x}_S)}{r_{\oplus}}, \quad (36)$$

where r_{\oplus} denotes the distance between the Earth and the source. The sole merit of this expression is to exhibit the importance of remote sources. We will therefore keep in mind that the antiproton sphere is much more extended than for positrons. The finite thickness of the diffusive halo is nevertheless a limiting factor since cosmic rays may escape through the vertical boundaries as they wander towards the Earth. As a consequence, the size of the antiproton sphere cannot be much larger than the DH half-thickness L . Galactic convection comes also into play. If the wind velocity V_C is large, cosmic rays are efficiently blown outside the Milky Way. This process limits further the reach of the antiproton sphere. The solution of the master equation (23) has been thoroughly investigated and several different techniques (Maurin et al. 2006; Bringmann & Salati 2007) lead essentially to the same fluxes at the Earth. In the Green function formalism, the diffusive halo is pictured as an infinite slab with no radial boundaries. On the contrary, the Bessel expansion method takes advantage of the axial symmetry of the propagation region and enforces a vanishing cosmic ray flux at a distance $R = 20$ kpc from the rotation axis of the Milky Way.

Since energy losses and diffusive re-acceleration are negligible, the antiproton energy E_S at the source is equal to its energy E at the Earth. Expression (25) may be considerably

simplified into

$$\Phi_{\bar{p}}(\odot, E) = \mathcal{F} f(E) I(E), \quad (37)$$

where the halo integral I is now a function of the antiproton energy $E \equiv E_S$. The signal generated by the DM shells of Section 2 is enhanced with respect to the smooth distributions of Table 3 by the boost factor

$$B_{\bar{p}} \equiv I_{\text{shell}}^{\bar{p}}(E) / I_{\text{smooth}}^{\bar{p}}(E). \quad (38)$$

The latter is plotted in Fig. 7 as a function of the antiproton interstellar kinetic energy $T_{\bar{p}}^{\text{IS}}$ for the three propagation models of Table 2. A cut-off radius of 300 pc has been assumed for the DM shell distribution. Its boost $B_{\bar{p}}$ is calculated with respect to a smooth NFW halo. The Green function technique yields the long-dashed curves which are exactly superimposed on the solid lines derived with the Bessel expansion method. Energy losses and diffusive re-acceleration have been switched off as well as the production of tertiary antiprotons. The MAX propagation model (red curve) is characterized by a large value of the half-thickness L and a small convection velocity V_C . The antiproton sphere spreads therefore over a large portion of the Milky Way and reaches the inner dense regions of its DM halo. The boost factor is essentially constant and is equal to ~ 30 above a few GeV. For exactly the opposite reasons, the MIN configuration (blue line) does not lead to any enhancement of the antiproton signal in the presence of DM caustics. The diffusive halo is too thin and the galactic wind too strong to let the antiprotons originating from the galactic centre to reach the Earth. The MED case (in green) features the intermediate situation. Above ~ 100 GeV, diffusion takes over galactic convection and the antiproton sphere is essentially limited by the half-thickness L . It extends sufficiently close to the centre to become sensitive to its large DM density, hence a boost factor identical to the MAX result. Below ~ 10 GeV, the galactic wind is on the contrary strong enough to restrain the antiproton sphere from spreading and the MIN situation is recovered.

In Fig. 8, the MED propagation mode has been selected. The boost $B_{\bar{p}}$ is featured as a function of the antiproton interstellar kinetic energy $T_{\bar{p}}^{\text{IS}}$ for three different values of the cut-off radius $r_{\text{cut-off}}$. It has been normalized to a NFW profile (solid) or an isothermal cored distribution (long-dashed). The solid red curve of the left panel corresponds therefore to the green line of Fig. 7 and the decrease of the boost at low energy has been explained as a result of the galactic wind taking over diffusion. In the right panel, the Bessel expansion technique alone has been used in order to implement energy losses and diffusive re-acceleration. The inelastic and yet non-annihilating interaction of an antiproton with an hydrogen atom of the interstellar medium is possible through the production of a Δ resonance which subsequently decays into a proton and a pion. The antiproton is not destroyed but loses a significant portion of its energy in a single collision. This so-called tertiary process has also been taken into account in the right panel. The curves are significantly flattened since the low-energy tail of the spectrum is replenished by higher energy antiprotons undergoing these inelastic and non-annihilating scatterings. Since the energy E drifts now with respect to its initial value E_S , the injected spectrum matters. In the right panel, $f(E_S)$ has been assumed to be constant. This is an unrealistic situation as the antiproton

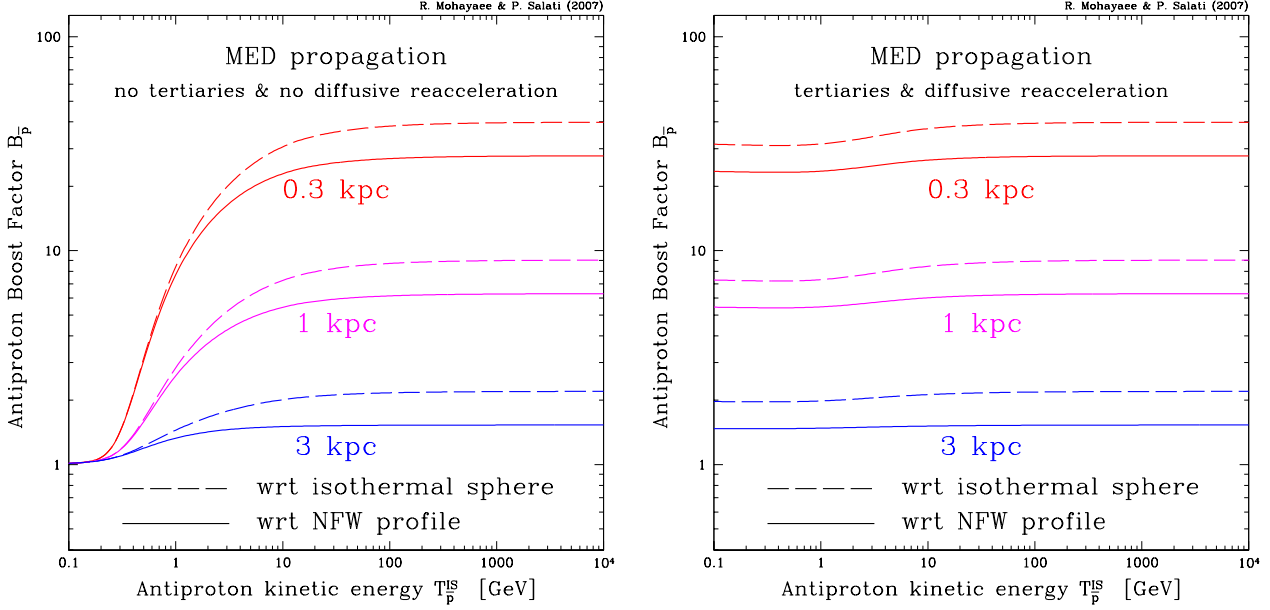


Figure 8. Antiproton boost factor in the presence of DM caustics normalized to a NFW profile (solid) or an isothermal cored distribution (long-dashed) in the case of the propagation model MED of Table 2. Three different values for the cut-off radius of the DM shell distribution have been considered. Energy losses and diffusive re-acceleration have been taken into account in the right panel as well as the production of tertiary antiprotons which induces a dramatic increase of the boost at low energy.

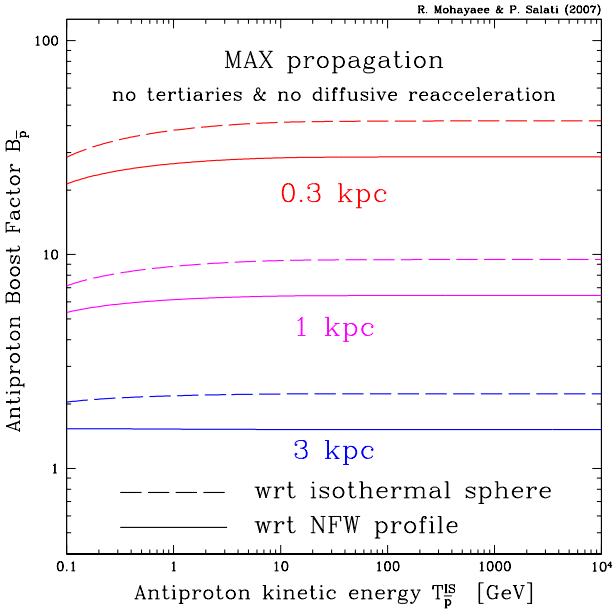


Figure 9. Same plot as the left panel of Fig. 8 where the propagation model is now the MAX configuration of Table 2.

spectrum generated by WIMP annihilation is expected to be softer than a flat distribution. The panels of Fig. 8 feature therefore two extreme trends and the actual boost should follow an intermediate behaviour.

In Fig. 9, energy losses and diffusive re-acceleration have been switched off as well as the above mentioned tertiary process. The situation is therefore similar to what has been

assumed in the left panel of Fig. 8 up to the propagation model which is now the MAX configuration of Table 2. The right panel of Fig. 8 (MED propagation with tertiaries and diffusive re-acceleration) is similar to Fig. 9 (MAX propagation without tertiaries nor diffusive re-acceleration). We conclude that in the MED configuration, the antiproton horizon may be somewhat stretched at low energy by the tertiary process which allows a fraction of the high energy antiprotons to make it from the inner Galaxy to the Earth where they subsequently populate the energy band below ~ 10 GeV.

To illustrate the cosmic ray signature of DM caustics, we have selected the case of a 1.7 TeV Wino. This species is expected for example in anomaly mediated supersymmetry breaking (AMSB) scenarios (Ullio 2001). Relic density requirements point towards a mass of 1.7 TeV (Profumo & Yaguna 2004). Non-perturbative, binding energy effects imply a greatly enhanced annihilation cross section today, when these species have very small galactic velocities as shown by Hisano et al. (2005). In Fig. 10, a value of $1.02 \times 10^{-24} \text{ cm}^3 \text{ s}^{-1}$ has been assumed for $\langle \sigma_{\text{ann}} v \rangle$. In this limit, heavy Winos annihilate almost exclusively into gauge bosons, with a branching ratio of 80% into W^+W^- pairs and of 20% into Z^0Z^0 pairs in our example. In the left panel, the antiproton spectrum is plotted as a function of the antiproton kinetic energy. The MED propagation mode is selected here and since in that case the antiproton horizon is fairly limited at low energy, the yield from DM annihilation is small and compatible with the measurements. Above ~ 10 GeV, the signal however increases dramatically with respect to the background (yellow band) which consists of secondary antiprotons. The latter are produced conventionally by the spallations of high-energy CR nuclei on the inter-

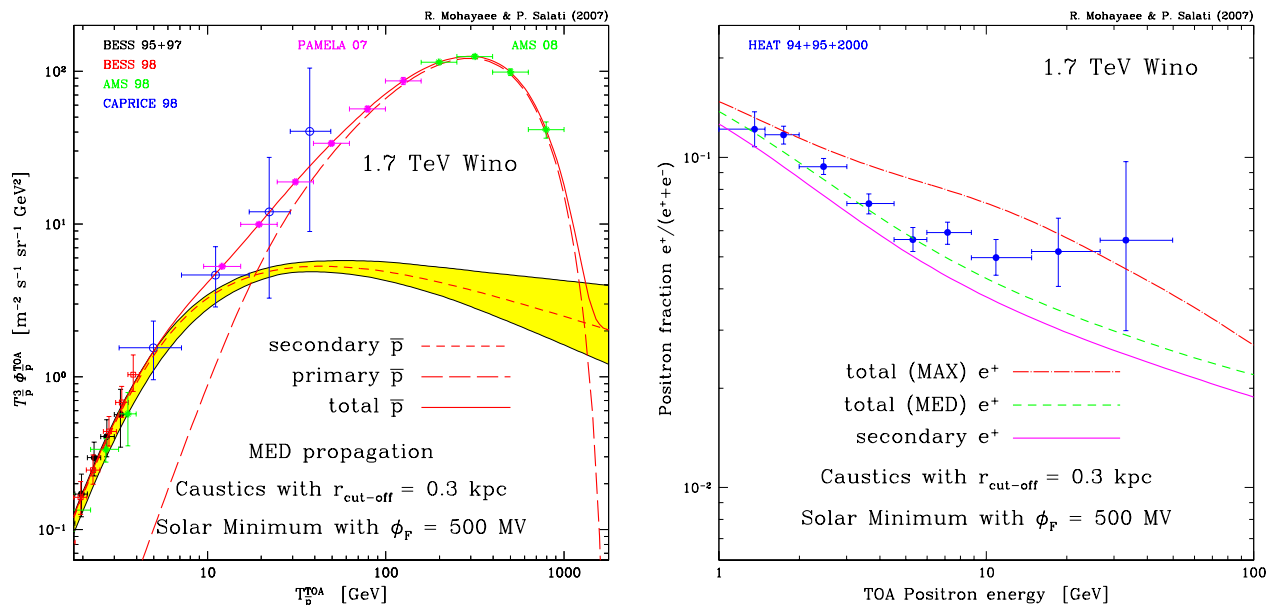


Figure 10. Signals expected in the case of a 1.7 TeV Wino and a DM shell distribution with a cut-off radius of 300 pc. In the left panel, the antiproton flux $T_p^3 \phi_p^{\text{TOA}}$ is plotted as a function of the antiproton kinetic energy T_p^{TOA} and compared to several measurements (Orito et al. 2000; Maeno et al. 2001; Boezio et al. 2001; Aguilar et al. 2002) and projected observations (Picozza et al. 2007; Barao 2004). The MED propagation model has been assumed. In the right panel, the positron fraction is featured for the MAX and MED propagation sets together with the HEAT data (Barwick et al. 1997).

stellar gas. The solid red curve is even compatible with the CAPRICE data (Boezio et al. 2001) which possibly hint at a spectral distortion. The largest discrepancy between the DM shell signal and the secondary background is reached for an energy of 300 GeV. The antiproton sphere clearly reaches the core of the DM shell distribution. Notice that no artificial enhancement of the antiproton primary flux is necessary here. We have used solely the DM distribution resulting from the self-similar infall model of Section 2 with no extra boost factor. Our only assumption is a cut-off radius of 0.3 kpc. In the right panel, the positron fraction is presented as a function of the positron energy E at the Earth. The solid magenta curve corresponds to the background alone as derived in (Moskalenko & Strong 1998). Secondary positrons are produced in the Galaxy from the collisions of cosmic ray proton and helium nuclei on the interstellar medium. The short-dashed green line features the signal of the 1.7 TeV Wino under scrutiny and is based on the MED propagation mode. The positron sphere is sensitive to the high DM density of the central caustics only at low energy, in a regime where the secondary background is large enough to hide easily a spectral distortion. This is no longer the case if the MAX propagation model is substituted for the MED configuration. The positron sphere becomes large enough to reach the galactic centre below 50 GeV and the long-dashed red curve exhibits a clear excess with respect to the background. The HEAT measurements (Barwick et al. 1997) are not well reproduced though. They point towards a positron excess which increases above 10 GeV, a trend which our shell density (30) clearly does not match. A Kaluza-Klein DM species with a substantial positron line has been invoked to fit the HEAT distortion (Cheng et al. 2002; Hooper & Silk 2005). However, an artificial boost factor of $5 \times (0.43/0.3)^2 \sim 10$ on

the entire positron energy range is necessary. Another possibility relies on the presence of high concentrations of WIMPs in the solar neighbourhood. The increase of the HEAT excess with energy indicates that a local mechanism is at play. The probability for a DM clump to be close to the Earth has been investigated (Hooper et al. 2004; Lavalle et al. 2007a). In our case, the caustics themselves could play the same role as the clumps insofar as the DM density reaches there a priori extreme values. We may wonder then how large the positron signal could be, should the solar system be close to one of these shells.

4 DARK MATTER DRAPERIES AND THE POSITRON EXCESS

Unlike antiprotons which have a very long diffusion length, the positrons that are detected at the Earth before significantly losing their energy ($E \simeq E_S$) have covered on average a small distance. For this reason, they can be important tracers of nearby density peak structures such as the dark matter “draperies” on which we focus here. As mentioned in Section 3, the solar system is located between two nearby shells. In our self-similar infall model, the 58th and 59th caustics lie respectively at a distance of 8.0916 and 7.9599 kpc from the galactic centre. The shell separation $e = r_{58} - r_{59}$ is equal to 131.7 pc. It is 8 orders of magnitude larger than the shell thickness for which a typical value is given by $\Delta r_{58} = 4.4 \times 10^7 \text{ km}$, hence the term “drapery”. A turnaround radius r_{ta} of 2.7854 Mpc has been obtained by setting the linearly-averaged density $\bar{\rho} = \rho_{\text{LE}} + \bar{\rho}_{58}$ equal to the solar neighbourhood value $\rho_{\odot} = 0.3 \text{ GeV cm}^{-3}$. The density ρ_{58} of the 58th caustic reaches a maximum of

$\rho_{58,\max} = 18.5 \text{ GeV cm}^{-3}$ inside an homogeneous slab whose thickness Δr_{58} is smaller than the distance between the Sun and Mercury. Should the Earth wander in this region of highly concentrated DM, the positron signal would be enhanced by a factor of $(\rho_{58,\max}/\rho_{\odot})^2 \sim 3,800$, hence the importance of exploring this possibility in greater detail.

To start, we note that changing slightly the value of ρ_{\odot} modifies the turnaround radius and affects the relative position of the solar system and the DM shells. The Earth may lie within the densest region of a caustic but the probability for such a situation is grossly given by the ratio $\epsilon_{58} = \Delta r_{58}/e \sim 10^{-8}$ and is vanishingly small.

Playing the devil's advocate, let us nevertheless assume that the solar system is indeed embedded inside this density peak region with typical DM density $\rho_{58,\max}$. Should this be the case, the positron signal would still be so smeared by diffusion and energy losses that it would be marginally enhanced with respect to the results presented in Section 3. Even in the extreme situation of a line where the injection energy is $E_S = m_{\chi}$, positrons are detected at energies $E < E_S$ and originate from a sphere all the more extended as the energy difference $\Delta E = E_S - E$ is large. Let us consider the MED propagation model for which the spectral index of the diffusion coefficient K is $\delta = 0.7$. In the limit where the energy difference ΔE is small compared to the positron energy $E \simeq E_S$, we may differentiate relation (34) and combine the result with definition (33) to get

$$\lambda_D = 3.77 \text{ kpc } \Delta \epsilon^{1/2} \epsilon_S^{-0.65} , \quad (39)$$

where $\epsilon_S = E_S/E_0$ and $E_0 = 1 \text{ GeV}$. For a typical positron energy of 100 GeV , the diffusion length is equal to

$$\lambda_D = 1.89 \text{ kpc } \sqrt{\frac{\Delta E}{E_S}} , \quad (40)$$

Because the experimental determination of the energy E is performed with a limited accuracy, positrons emitted monochromatically at $E_S = 100 \text{ GeV}$ are collected in an energy band set by the resolution of the instrument. Even in the optimistic case where energy is measured at the 1% level, *i.e.* with $\Delta E/E_S = 10^{-2}$, relation (40) yields a positron sphere which reaches as far as 190 pc from the Earth at $E = 99 \text{ GeV}$. The signal collected in the energy bin of the line does not originate solely from the densest part of the caustic. It has been produced from a much more extended zone whose average DM density is

$$\bar{\rho} \simeq \rho_{LE} \simeq \rho_{\odot} = 0.3 \text{ GeV cm}^{-3} . \quad (41)$$

Remember that if the shells are dense, they are also extremely thin. The DM density ρ_{58} for instance undergoes a discontinuity at the external boundary of the 58th caustic and drops so violently inwards that it decreases from 18.5 down to 0.3 GeV cm^{-3} on a distance of $5.4 \times 10^{-3} \text{ pc}$ only. Averaged over a distance D , this density is given by

$$\bar{\rho}_{58} = 2 \rho_{58,\max} \sqrt{\frac{\Delta r_{58}}{D}} , \quad (42)$$

where relation (28) has been used. For a distance $D = 1 \text{ pc}$, we get a value of $0.044 \text{ GeV cm}^{-3}$ which barely represents 15% of the solar neighbourhood value. Averaged now over the distance e separating two nearby shells, it amounts to 1.3% of the density ρ_{\odot} , in agreement with the relative positions of the long-dashed dotted red curve (averaged total

DM density) and the short-dashed blue line (lower envelope) of Fig. 4.

In order to elaborate on the smearing of the positron horizon by the limited resolution of energy measurements, some modelling is necessary. Since the shells are extremely thin, we will replace the actual DM density by the fine-grained distribution ρ_{eff} where

$$\frac{\rho_{\text{eff}}^2}{\rho_{\odot}^2} = \frac{\rho_{LE}^2}{\rho_{\odot}^2} + \sum_{\text{shells } k} A e \delta(z - z_k) . \quad (43)$$

The shells are now pictured as infinitely thin slabs located at the positions $z = z_k$ on the radial axis connecting the galactic centre to the Earth. They are separated from each other by the distance e defined above. Setting the total number of DM annihilations constant, the parameter A is found to be equal to

$$A = \frac{\bar{\rho}^2 - \rho_{LE}^2}{\rho_{\odot}^2} \simeq 2 \frac{\bar{\rho}_{58}}{\rho_{\odot}} , \quad (44)$$

with a typical value of 0.0263. The effect which we discuss here is the strongest in the case of a positron line for which the injection spectrum is $f(E_S) = \delta(E_S - m_{\chi})$. The positron flux at the Earth is given by the product

$$\Phi_{e^+}(\odot, E) = \mathcal{F} I^{e^+}(E, E_S = m_{\chi}) , \quad (45)$$

where the halo integral I^{e^+} is the convolution (27) between the DM density and the positron Green function G_{e^+} . Close to the line energy, for $E \simeq m_{\chi}$, the positron horizon is so limited that we may not replace the actual DM density by its coarse-grained average (30), especially if the Earth lies in the region where the caustic density is the highest. The results presented in Section 3 should potentially vary if we compute now the halo integral I^{e^+} with the fine-grained density (43). The relative change in the positron flux is equal to the ratio

$$\frac{\delta I^{e^+}}{I^{e^+}} \equiv \frac{I_{\text{fine}}^{e^+} - I_{\text{coarse}}^{e^+}}{I_{\text{coarse}}^{e^+}} . \quad (46)$$

Because the positron propagator may be expressed as

$$G_{e^+}(\mathbf{x}, E \leftarrow \mathbf{x}_S, E_S) = \frac{\tau E}{E_0 \epsilon^2} \tilde{G}(\mathbf{x} \leftarrow \mathbf{x}_S; \lambda_D) , \quad (47)$$

the halo integral I^{e^+} is related to the convolution \tilde{I} of the DM density with the heat Green function \tilde{G} through

$$I^{e^+}(E, E_S) \equiv \frac{\tau E}{E_0 \epsilon^2} \tilde{I}(\lambda_D) , \quad (48)$$

where

$$\tilde{I}(\lambda_D) = \int_{\text{DH}} d^3 \mathbf{x}_S \tilde{G}(\mathbf{x}_{\odot} \leftarrow \mathbf{x}_S; \lambda_D) \left\{ \frac{\rho(\mathbf{x}_S)}{\rho_{\odot}} \right\}^2 . \quad (49)$$

Considering the fine-grained DM distribution (43) instead of the coarse-grained average (30) induces a relative change in the positron flux equal to $\delta \tilde{I}/\tilde{I}_{\text{coarse}}$ where

$$\delta \tilde{I} \equiv \tilde{I}_{\text{fine}} - \tilde{I}_{\text{coarse}} , \quad (50)$$

and

$$\tilde{I}_{\text{coarse}} = \int_{\text{DH}} d^3 \mathbf{x}_S \tilde{G}(\mathbf{x}_{\odot} \leftarrow \mathbf{x}_S; \lambda_D) \frac{\bar{\rho}^2}{\rho_{\odot}^2} . \quad (51)$$

We are interested here in the limit where the positron diffusion length λ_D is small compared to the intershell separation $e \sim 132 \text{ pc}$. In this regime, λ_D is much smaller than the

DH half-thickness L and the heat Green function \tilde{G} simplifies into (Baltz & Edsjö 1999; Lavalle et al. 2007a)

$$\tilde{G}(\mathbf{x} \leftarrow \mathbf{x}_S; \lambda_D) = \frac{1}{\pi^{3/2} \lambda_D^3} \exp\left\{-\frac{(\mathbf{x} - \mathbf{x}_S)^2}{\lambda_D^2}\right\}. \quad (52)$$

Since $\overline{\rho^2} \simeq \rho_\odot^2$, we are led to the conclusion that $\tilde{I}_{\text{coarse}} \simeq 1$. Our task consists simply in evaluating the difference

$$\delta\tilde{I}(\lambda_D) = \int_{\text{DH}} d^3\mathbf{x}_S \tilde{G}(\mathbf{x}_\odot \leftarrow \mathbf{x}_S; \lambda_D) \left\{ \frac{\rho_{\text{eff}}^2 - \overline{\rho^2}}{\rho_\odot^2} \right\}, \quad (53)$$

and in comparing it to unity. With our fine-grained expression (43), this integral becomes

$$\delta\tilde{I}(\lambda_D) = \int_{\text{DH}} d^3\mathbf{x}_S \tilde{G} A \left\{ -1 + \sum_{\text{shells } k} e \delta(z - z_k) \right\}. \quad (54)$$

To proceed further, we simplify the Gaussian expression (52) for the heat propagator \tilde{G} into the step function

$$\tilde{G} = \frac{1}{V_D} \theta(\lambda_D - r_\oplus), \quad (55)$$

where r_\oplus denotes the distance of the source to the Earth. The radius of the positron sphere is λ_D and its volume is $V_D = 4\pi\lambda_D^3/3$. We readily find that

$$\delta\tilde{I}(\lambda_D) = A \left\{ -1 + \sum_{-\lambda_D \leq z_k \leq \lambda_D} \frac{\pi e}{V_D} (\lambda_D^2 - z_k^2) \right\}, \quad (56)$$

where the sum runs over the DM shells that intersect the positron sphere. In the limit where the positron diffusion length λ_D is much larger than the caustic separation e , the difference $\delta\tilde{I}$ vanishes as expected. In this regime, the positron sphere is so large that the coarse-grained density (30) is enough to describe appropriately the DM distribution. We are actually interested here in the opposite limit where the ratio λ_D/e is small and where the draperies come into play. The difference $\delta\tilde{I}$ may be conveniently expressed as

$$\delta\tilde{I}(\lambda_D) = A \frac{e}{\lambda_D} \mathcal{D}, \quad (57)$$

where the drapery function \mathcal{D} is defined as

$$\mathcal{D} \equiv -\frac{\lambda_D}{e} + \sum_{-\lambda_D \leq z_k \leq \lambda_D} \frac{3}{4} \left(1 - \frac{z_k^2}{\lambda_D^2}\right). \quad (58)$$

The latter is plotted in Fig. 11 as a function of the ratio λ_D/e . The minimal value of the difference $\delta\tilde{I}$ is reached when no DM shell intersects the positron sphere. The Earth lies between two nearby draperies. This case is featured for instance by the short-dashed green and long-dashed dotted blue curves of Fig. 11 and provided that the positron diffusion length λ_D is small enough. The minimal value of $\delta\tilde{I}$ is equal to $-A$ and is negligible with respect to $\tilde{I}_{\text{coarse}} \simeq 1$. More complicated is the maximal configuration for which the Earth lies exactly inside a drapery and where the DM density is the highest. This case corresponds to the solid red line of Fig. 11. For very small values of the ratio λ_D/e , the drapery function \mathcal{D} is equal to $3/4$ and the difference $\delta\tilde{I}$ diverges like

$$\delta\tilde{I} = \frac{3A}{4} \frac{e}{\lambda_D}. \quad (59)$$

Because the energy is measured with a limited accuracy, the

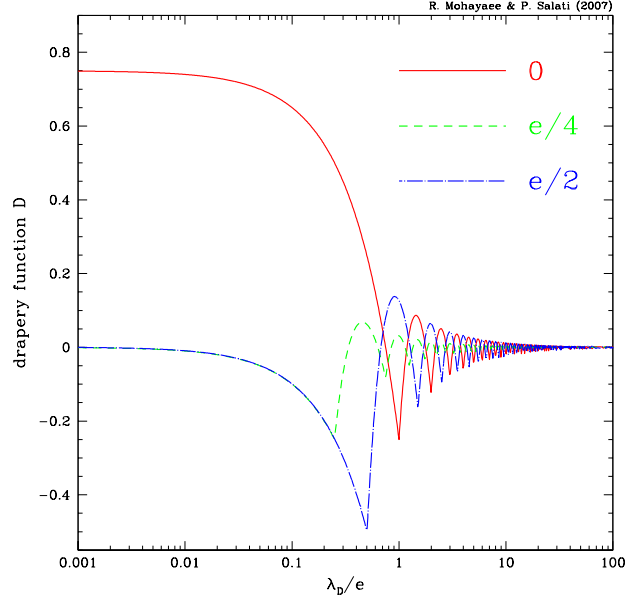


Figure 11. The drapery function \mathcal{D} is plotted against the ratio λ_D/e for three different values of the distance to the nearest DM shell. The solid red curve features the case where the Earth is located exactly inside a drapery and where the DM density is the highest. The integral $\delta\tilde{I}$ is maximal. The long-dashed dotted blue line corresponds to the opposite situation where the Earth lies at mid-distance between two caustics. The integral $\delta\tilde{I}$ is minimal with a negative value. The intermediate situation for which the nearest shell is located at a distance of $e/4$ leads to the short-dashed green curve.

relevant quantity is the averaged value of the difference $\delta\tilde{I}$ which we define as

$$\delta\tilde{I}_{\Delta E} = \frac{1}{\Delta E} \int_{E_S - \Delta E}^{E_S} dE \delta\tilde{I}(\lambda_D). \quad (60)$$

This integral is performed on the energy bin that contains the line at $E_S = m_\chi$. Close to the line, *i.e.* for $E \simeq E_S$, the positron diffusion length λ_D is given by expression (39) which we combine with relation (59) to get

$$\delta\tilde{I}_{\Delta E} = \frac{3A}{2} \left(\frac{e}{3.77 \text{ kpc}} \right) \frac{\epsilon_S^{0.65}}{\sqrt{\Delta\epsilon}}. \quad (61)$$

For a 100 GeV DM species, this leads to a difference between the fine-grained and coarse-grained halo integrals of

$$\delta\tilde{I}_{\Delta E} = 2.75 \times 10^{-3} \sqrt{\frac{E_S}{\Delta E}}. \quad (62)$$

A 1% measurement of the energy translates into a maximal value of the difference $\delta\tilde{I}_{\Delta E}$ of $0.0275 \sim 3\%$. We therefore conclude that even in the worst situation where the Earth lies in the region of highest DM density, we find no difference between the results of Section 3 and those derived with the fine-grained distribution (43) once the energy is properly averaged.

5 CONCLUSIONS

We have studied whether DM caustics in the halo of the Milky Way can amplify the flux of cosmic ray antipro-

tons and positrons which is received at the Earth. We have used the secondary infall model for our halo which naturally includes the caustics and assumed that the galactic DM is made of weakly interacting massive species. We have then taken into account the smearing of the caustics due to a present-day velocity dispersion of these particles of 0.03 cm s^{-1} .

The cosmic ray antiprotons and positrons that are detected at the Earth originate from a region whose typical size is much larger than the shell thickness or even the shell separation. This particle horizon probes a large portion of the Milky Way and the coarse-grained average density (30) provides an adequate description. In the solar neighbourhood, the coarse-grained caustic density is the same as the smooth NFW or isothermal cored distributions usually assumed in the literature. The difference lies at the center of the Milky Way. The lower-envelope density diverges there with an index of ~ 2.11 , hence a DM profile steeper than even in the NFW case. The coarse-grained shell density is assumed to be constant inside a sphere of radius $r_{\text{cut-off}}$ whose value is unknown. The smaller this cut-off radius, the more abundant DM at the galactic center and consequently the stronger its signal should it reach the Earth.

We have then computed the antiproton flux which the coarse-grained shell density yields at the Earth. The reach of the antiproton sphere depends on the cosmic ray propagation model but is always of order a few kiloparsecs. The MIN configuration is associated to a rather small antiproton range. The associated signal is not different from what is derived assuming NFW or isothermal cored distributions. The MAX propagation model is characterized on the contrary by efficient diffusion taking over a moderate galactic convection. The antiproton sphere probes the inner and denser regions of the Milky Way. We find that the antiproton signal is enhanced by a factor of ~ 30 should the conventional smooth NFW profile be replaced by the coarse-grained shell density (30) for which a cut-off radius of 300 pc has been assumed. The MED set of propagation parameters corresponds to the best fit to the B/C data and features the intermediate situation. It leads to the exciting possibility that the antiproton signal is only boosted above 10 GeV in the presence of caustics. Depending on the WIMP annihilation cross section, the antiproton flux could be severely distorted at high energy as shown in Fig. 10 where no artificial boost factor is required. Thus a promising window opens up around a few hundreds of GeV where future antiproton measurements are eagerly awaited.

We are less optimistic for the positron signal. Depending on the cosmic ray propagation model, the positron flux at the Earth may be enhanced in the presence of shells with respect to a smooth NFW or isothermal cored DM profile. However, this situation arises only at low energy where the observations are already well explained by the sole secondary background component. Thus DM caustics cannot provide an explanation for the HEAT excess reported above ~ 10 GeV and consequently produced in the solar neighbourhood. The solution so far invoked is based on a WIMP with a hard positron annihilation spectrum like a Kaluza-Klein particle (Cheng et al. 2002) or a neutralino with a dominant W^+W^- channel (Hooper & Silk 2005; Delahaye et al. 2007). Boost factors of ~ 10 with respect to a smooth NFW DM halo are nevertheless necessary. Such a value is marginally possible

(Lavalle et al. 2007b) in scenarios inspired by the Λ -CDM N-body numerical simulations which point towards the existence of numerous and dense DM clumps inside which WIMP annihilation can be enhanced. We showed that the coarse-grained shell density (30) does not provide an alternative to explaining the HEAT excess. However, further data with higher precision and also a better understanding of the secondary positron background are needed to firmly exclude caustics as a possible explanation of the HEAT measurements. It remains very unlikely nevertheless that the present spectral form could be reproduced by caustics, at least by its coarse-grained distribution (30).

We finally explored the possibility that the fine-grained distribution (43) could yield a strong positron flux should the Earth be embedded inside the densest part of a caustic, a region where the DM density reaches its peak value $\rho_{k,\text{max}}$. At high energy, the positron sphere shrinks. Averaging the fine-grained shell density (13) by its coarse-grained approximation (30) is no longer possible. Positrons that are received at the Earth have short diffusion lengths λ_D and hence can be excellent tracers of nearby caustics. We investigated here the case of a positron line. Positrons that are detected exactly at the line energy $E = E_S \equiv m_\chi$ have vanishing diffusion length and if the Earth sits exactly inside the shell, an enhancement of the positron signal by a factor of $\sim 3,800$ is naively expected. However, energy is measured with a limited accuracy and the energy bin of the line has a non-vanishing width. Averaging λ_D over the line bin leads to a diffusion length which is still far larger than the typical caustic thickness or even separation. Our study showed no difference between the results of Section 3 and those derived with the fine-grained distribution (43) once energy is properly averaged. We hypothesize that an extremely high energy resolution, presently unavailable, would allow to detect the nearby caustics.

A word of caution is necessary at this stage though. The analysis of Section 4 is based on the assumption that cosmic rays diffuse on the inhomogeneities of the galactic magnetic field. The mean free path λ_{free} of their random walk may be derived from the space diffusion coefficient K through the canonical relation

$$K(E) \equiv \frac{1}{3} \lambda_{\text{free}} \beta . \quad (63)$$

In this diffusion scheme and with the MED set of parameters, positrons with energy ϵ cover on average a distance

$$\lambda_{\text{free}} = 1.1 \times 10^{-4} \text{ kpc } \epsilon^{0.7} \quad (64)$$

before their next scattering on Alfvén waves. Our treatment of cosmic ray propagation is definitely supported by the fact that λ_{free} is much smaller than the horizon size set by λ_D and equation (39). However, if the nearest DM caustic is very close to the Earth and lies at a distance which does not exceed λ_{free} or if the Earth is embedded inside the densest part of a shell, the diffusion hypothesis breaks down. Positrons will essentially drift along the lines of the magnetic field without encountering on their way any obstacle. Depending on the relative orientation of the local magnetic field with respect to the Earth and its nearest caustic, we could be possibly exposed to an intense high-energy positron flux whose evaluation is clearly beyond the scope of this article.

Acknowledgment : We thank Pierre Brun and Julien Lavalle

for having provided us with a few typical positron and antiproton spectra arising from WIMP annihilation. RM thanks Sergei Shandarin for contributions, Niayesh Afshordi, Ed Bertschinger and Mike Kuhlen for discussions and LAPTH Annecy for hospitality and French programmes PNC & ANR (OTARIE) for travel grants.

REFERENCES

Aguilar M., et al., 2002, *Phys. Rept.*, 366, 331
 Alard C., Colombi S., 2005, *MNRAS*, 359, 123
 Ascasibar Y., Hoffman Y., Gottlöber S., 2007, *MNRAS*, 376, 393
 Bahcall J. N., Soneira R. M., 1980, *Astrophys. J. Suppl.*, 44, 73
 Baltz E. A., Edsjö J., 1999, *Phys. Rev.*, D59, 023511
 Barao F., 2004, *Nucl. Instrum. Meth.*, A535, 134
 Barwick S. W., et al., 1997, *Astrophys. J.*, 482, L191
 Bertschinger E., 1985, *ApJS*, 58, 39
 Boezio M., et al., 2001, *Astrophys. J.*, 561, 787
 Bringmann T., Salati P., 2007, *Phys. Rev.*, D75, 083006
 Carter D., Allen D. A., Malin D. F., 1982, *Nature*, 295, 126
 Casse F., Lemoine M., Pelletier G., 2002, *Phys. Rev.*, D65, 023002
 Cheng H.-C., Feng J. L., Matchev K. T., 2002, *Phys. Rev. Lett.*, 89, 211301
 Delahaye T., Lineros R., Donato F., Fornengo N., Salati P., 2007, *astro-ph/0712.2312*
 Diemand J., Moore B., Stadel J., 2004, *MNRAS*, 353, 624
 Donato F., et al., 2001, *Astrophys. J.*, 563, 172
 Donato F., Fornengo N., Maurin D., Salati P., Taillet R., 2004, *Phys. Rev.*, D69, 063501
 Fillmore J. A., Goldreich P., 1984, *ApJ*, 281, 1
 Gott J. R. I., 1975, *ApJ*, 201, 296
 Gunn J. E., 1977, *ApJ*, 218, 592
 Hayashi E., Navarro J. F., Taylor J. E., Stadel J., Quinn T., 2003, *ApJ*, 584, 541
 Hernquist L., Quinn P. J., 1988, *ApJ*, 331, 682
 Hernquist L., Quinn P. J., 1989, *ApJ*, 342, 1
 Hisano J., Matsumoto S., Nojiri M. M., Saito O., 2005, *Phys. Rev.*, D71, 063528
 Hooper D., Silk J., 2005, *Phys. Rev.*, D71, 083503
 Hooper D., Taylor J. E., Silk J., 2004, *Phys. Rev.*, D69, 103509
 Lavalley J., Pochon J., Salati P., Taillet R., 2007a, *Astronomy & Astrophysics*, 462, 827
 Lavalley J., Yuan Q., Maurin D., Bi X., 2007b, *astro-ph/0709.3634*
 Maeno T., et al., 2001, *Astropart. Phys.*, 16, 121
 Malin D. F., Carter D., 1980, *Nature*, 285, 643
 Maurin D., Donato F., Taillet R., Salati P., 2001, *Astrophys. J.*, 555, 585
 Maurin D., et al., 2002, *astro-ph/0212111*
 Maurin D., Taillet R., Combet C., 2006, *astro-ph/0609522*
 Mohayaee R., Shandarin S. F., 2006, *MNRAS*, 366, 1217
 Moskalenko I. V., Strong A. W., 1998, *Astrophys. J.*, 493, 694
 Natarajan A., Sikivie P., 2006, *Phys. Rev.*, D73, 023510
 Navarro J. F., Frenk C. S., White S. D. M., 1997, *Astrophys. J.*, 490, 493
 Orito S., et al., 2000, *Phys. Rev. Lett.*, 84, 1078

Picozza P., et al., 2007, *Astropart. Phys.*, 27, 296
 Profumo S., Yaguna C. E., 2004, *Phys. Rev.*, D70, 095004
 Sikivie P., Ipser J. R., 1992, *Physics Letters B*, 291, 288
 Sikivie P., Tkachev I. I., Wang Y., 1997, *Phys. Rev.*, D56, 1863
 Tremaine S., 1999, *MNRAS*, 307, 877
 Ullio P., 2001, *JHEP*, 06, 053
 Vogelsberger M., White S. D. M., Helmi A., Springel V., 2007, *astro-ph/0711.1105*; submitted to *MNRAS*